Ab initio study of electronic excitations and the dielectric function in molybdenum disulfide monolayer

Despoja, Vito; Rukelj, Zoran; Marušić, Leonardo

Ab initio study of electronic excitations and the dielectric function in molybdenum disulfide monolayer

Vito Despoja,[1,*] Zoran Rukelj,[1] and Leonardo Marušić[2]
[1]*Department of Physics, University of Zagreb, Bijenička 32, HR-10000 Zagreb, Croatia*
[2]*Maritime Department, University of Zadar, M. Pavlinovića 1, HR-23000 Zadar, Croatia*
(Received 25 August 2016; published 26 October 2016)

The propagator of the induced dynamically screened Coulomb interaction $W^{\rm ind}(\mathbf{Q},\omega,z,z')$ is calculated for the MoS_2 monolayer. The energy-loss rate of a point charge placed near the MoS_2 monolayer is calculated (using the spatial resolution of the $W^{\rm ind}$ in the direction perpendicular to the MoS_2 plane) and successfully compared with very recent electron-energy-loss spectroscopy measurements of Hong *et al.* [J. Hong *et al.*, Phys. Rev. B **93**, 075440 (2016)]. The induced propagator $W^{\rm ind}$, compared with its classical analogous propagator, is used to determine the effective dielectric function $\epsilon_{\rm eff}(\omega)$ of atomically thick crystals. It is shown that $\epsilon_{\rm eff}(\omega)$ extracted from $W^{\rm ind}$ is in good agreement with the dielectric function of the MoS_2 extracted from the ellipsometry measurements. A recently proposed method for calculation of the dielectric tensor in quasi-two-dimensional crystals is used to calculate the parallel $\epsilon_{\parallel}(\omega)$ and perpendicular $\epsilon_{\perp}(\omega)$ dielectric functions in MoS_2, which are compared with some previous measurements and calculations.

DOI: 10.1103/PhysRevB.94.165446

I. INTRODUCTION

Transition-metal dichalcogenides (TMDCs) recently became widely studied systems because of their favorable structural, electronic, and optical properties. They can be prepared as stable monolayer (ML) crystals [1–3] with a direct band gap, known as quasi-two-dimensional (q2D) semiconductors. These days, the most common direct gap ML semiconductors are molybdenum disulfide (MoS_2-ML) [4,5] and hexagonal boron nitride (hBN-ML) [6–8], but their heterostructures in combination with graphene have recently been fabricated and investigated [9] as well. The structural stability and direct band gap make these materials suitable for many applications such as electronics, optoelectronics, light emitters, detectors, and photovoltaic devices [10–19]. For example, because of MoS_2-ML high absorption in the visible frequency range, it can be complementary to graphene, which has low absorption in the visible frequency range and high conductivity in the far-infrared region, and is therefore suitable for solar cell technology [20]. On the other hand, the interaction of longitudinal probe or excitations (e.g., charged particle, dipole, or excitons in molecule) with MoS_2-ML is still poorly investigated. Also, various studies of MoS_2-ML dielectric function give quite contradictory, or at least different, results [21–26].

The propagator of the dynamically screened Coulomb interaction $W^{\rm ind}(Q,\omega,z,z')$ and the complex dielectric function $\epsilon(\omega)$ are very useful theoretical tools for the study of charged particle-crystal or light-crystal interactions. In addition, the dielectric function also provides the connection between theory and experiment. In this paper, we use the imaginary part of the induced Coulomb propagator $W^{\rm ind}(Q,\omega,z,z')$ [27,28] to calculate the energy-loss rate of a blinking point charge placed in the vicinity of a MoS_2-ML as a function of the blinking frequency ω. Since the blinking point charge loses energy to various electronic excitations in the crystal, the $\mathrm{Im}W^{\rm ind}$ defines the spectrum of electronic excitations in MoS_2-ML which can also be related to electron-energy-loss spectroscopy (EELS) measurements. In EELS, the crystal (surface) is exposed to a beam of electrons with monochromatic kinetic energies which are inelastically scattered on various polar excitations in the crystal, such as optical phonons, interband and intraband electron-hole excitations, plasmon excitations, etc. This results in the final measured electron spectra no longer being monochromatic, but having satellites which represent the energy losses to various excitations. Here, we explain the origin of the particular features in excitation spectra of MoS_2-ML in detail, and compare it with very recent EELS measurements [29].

The theoretically obtained dielectric function is primarily related to EELS experiments, but it also provides useful information about the optical properties of crystals, such as optical absorption spectra, transmissivity, and reflectivity. At the same time, the complex dielectric function extracted from particular optical measurements defines a variety of crystal properties. High anisotropy of extremely thin q2D crystals results in a very ambiguous definition of its dielectric function. To analyze this, we first study the widely used "macroscopic" dielectric function $\epsilon_M(\omega)$ [30] (obtained by inverting the 3D dielectric matrix $1-V\chi$ in the reciprocal space), but we also introduce the 2D dielectric function $\epsilon_{2D}(\omega)$ obtained by averaging the nonlocal 3D response (over z and z') and reducing it to the $z=0$ plane. We compare the result for the 2D dielectric function ϵ_{2D} with the result obtained by using the recently proposed two-band effective tight-binding approximation (TBA) model [31]. We show that "average" dielectric functions ϵ_M and ϵ_{2D} coincide. However, they are not suitable for describing the dielectric properties of radically anisotropic q2D crystals.

Another definition arises from studying the response (induced polarizability $\mathbf{P}$) of q2D crystal to external homogeneous electrical field $\mathbf{E}$. Because of the strong crystal anisotropy, the response depends on the direction of the applied field, which enables decomposition into parallel (to the q2D crystal plane) $\epsilon_{\parallel}(\omega)$ and perpendicular $\epsilon_{\perp}(\omega)$ dielectric

*vito@phy.hr

function. We use our recently proposed theoretical formulation of the current-current response tensor $\Pi_{\mu\nu}(\omega)$ [32] to calculate these two dielectric functions [$\epsilon_{\parallel}(\omega)$ and $\epsilon_{\perp}(\omega)$] and compare the results with previous theoretical and experimental results [23–26].

Finally, we explore a definition arising from the analysis of the induced (reflected) potential $W^{\rm ind}(Q,\omega,z,z')$ [27], which is first calculated using the full quantum mechanical approach, and then treating the q2D crystal as a dielectric slab with sharp boundaries described by the "effective" dielectric function $\epsilon_{\rm eff}(\omega)$. We show that the dielectric function obtained in this way is in the best agreement with dielectric functions extracted from ellipsometry measurements [21,22].

In Sec. II, we present the methodology used to calculate the ground state, noninteracting electrons response function $\chi^0(\omega)$, and dynamically screened Coulomb interaction $W(\omega)$. We also briefly present the derivation of model dielectric functions $\epsilon_{2D}(\omega)$, $\epsilon_M(\omega)$, $\epsilon_{\perp}(\omega)$, $\epsilon_{\parallel}(\omega)$, and $\epsilon_{\rm eff}(\omega)$. In Sec. III, we analyze the spectra of electronic excitations in MoS_2-ML and compare them with EELS measurements. Then, we analyze the results for various model dielectric functions in MoS_2-ML and compare these results with each other as well as with corresponding measurements. In Sec. IV, we present the conclusion.

II. METHODOLOGY

A. Ground-state calculation

The first part of the calculation consists of determining the Kohn-Sham (KS) wave functions $\phi_{n\mathbf{K}}$ and energy levels $E_{n\mathbf{K}}$, i.e., band structure, of a MoS_2-ML. For calculation of the KS states, we use the plane-wave self-consistent field (PWSCF) density functional theory (DFT) code within the QUANTUM ESPRESSO (QE) package [33]. The core-electron interaction is approximated by the norm-conserving pseudopotentials [34], and the exchange-correlation (XC) potential by the Perdew-Zunger local density approximation (LDA) [35]. For the MoS_2-ML unit-cell constant, we use the experimental value of $a_{uc} = 5.972$ a.u. and the vertical separation between sulfur layers is 5.868 a.u. [36]. Since the code requires periodicity in the direction perpendicular to the ML as well, and we want to investigate just one MoS_2-ML, we formally observe a superlattice constructed of the periodically placed MLs. This means that the separation between the MLs in the superlattice can be arbitrary and is important only to the extent that there is no electronic density overlap between neighboring monolayers, since an overlap could modify the MoS_2-ML orbital and band structure. Therefore, considering that MoS_2-ML thickness from sulfur to sulfur atom is almost 12 a.u. and that electronic density thickness is about 15 a.u. (as can be seen in Fig. 2), we chose the separation between MoS_2-MLs to be $L = 5a_{uc} = 29.86$ a.u.

As shown in Fig. 1, we orient the reference frame so that the MoS_2 crystal is positioned in the x-y plane, the z direction is perpendicular to the crystal plane, and the Mo atomic layer occupies the $z = 0$ plane. The ground-state electronic density of the MoS_2-ML is calculated by using $12 \times 12 \times 1$ Monkhorst-Pack K-point mesh [37] for the first Brillouin zone (BZ), i.e., we use 31 special points in the irreducible Brillouin zone (BZ). For the plane-wave cutoff energy, we choose 50 Ry (680 eV).

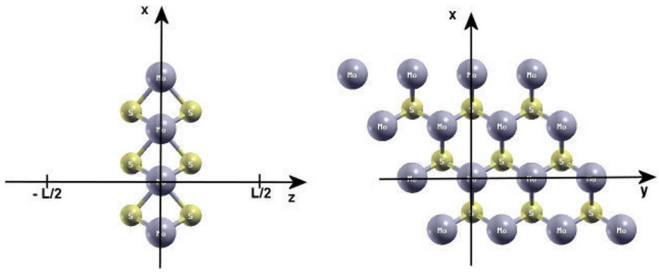

FIG. 1. Schematic representation of molybdenum disulfide monolayer. Molybdenum atomic layer (gray), surrounded by two sulfur atomic layers (yellow), occupies the $z = 0$ plane.

The MoS_2 ground-state electronic density profile

$$n(z) = \frac{2}{S} \sum_{\mathbf{K}\in S.B.Z.} \sum_{n} f_n(\mathbf{K}) \int_S d\boldsymbol{\rho} |\phi_{n\mathbf{K}}(\boldsymbol{\rho},z)|^2, \qquad (1)$$

where S is the normalization surface and $f_n(\mathbf{K}) = \theta[E_F - E_n(\mathbf{K})]$ is the Fermi-Dirac distribution at $T = 0$, is shown in Fig. 2(a). For the effective positive background thickness, we take $a = 8.93$ a.u., which corresponds to three times the separation between S and Mo layers in bulk MoS_2. The positive background density is then determined from the charge neutrality condition $n^+ = \frac{N_{el}}{aS_{uc}}$, where the number of valence electrons is $N_{el} = 18$ and the area of the surface unit cell is $S_{uc} = 30.88$ a.u.

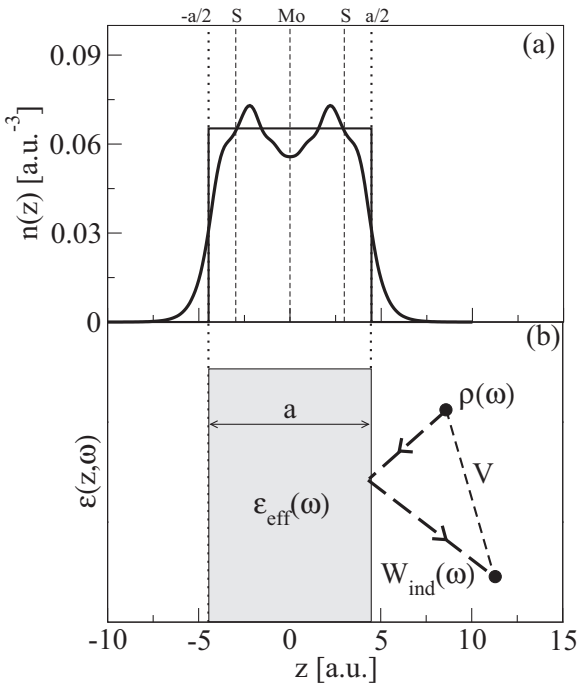

FIG. 2. (a) Ground-state electronic density profile [Eq. (1)] in MoS_2-ML; the rectangle represents the thickness of the effective positive background. (b) The schematic representation of the MoS_2 dielectric slab of thickness a.

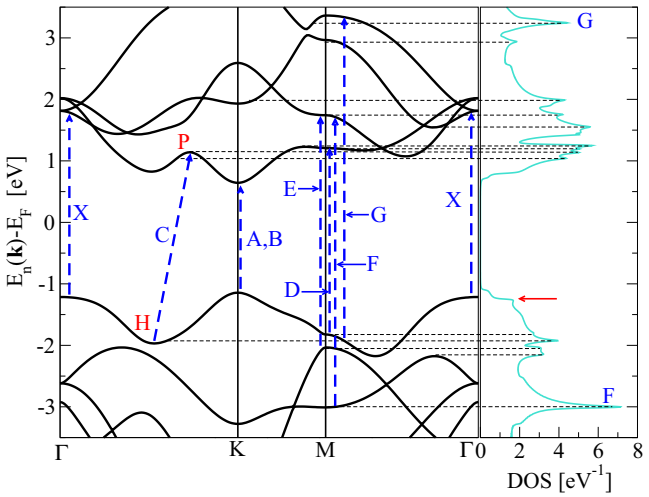

FIG. 3. The MoS_2-ML band structure (left panel) and DOS (right panel).

The MoS_2 band structure along the high-symmetry $\Gamma \rightarrow K \rightarrow M \rightarrow \Gamma$ directions shown in Fig. 3 is calculated along the path with 201 k points.

The MoS_2-ML density of states (DOS),

$$\mathrm{DOS}(E) = \frac{2}{S} \sum_{\mathbf{K} \in S.B.Z.} \sum_{n} \delta(E - E_{n,\mathbf{K}}),$$

shown in the right panel of Fig. 3, is calculated for denser 1 BZ K-point mesh sampling $401 \times 401 \times 1$ in order to achieve better resolution.

B. Response-function calculation

The 3D Fourier transform of the independent electron response function, or the random-phase approximation (RPA) irreducible polarizability [38], is given by

$$\chi^0_{\mathbf{G}\mathbf{G}'}(\mathbf{Q},\omega) = \frac{2}{\Omega} \sum_{\mathbf{K} \in S.B.Z.} \sum_{n,m} \frac{f_n(\mathbf{K}) - f_m(\mathbf{K}+\mathbf{Q})}{\omega + i\eta + E_n(\mathbf{K}) - E_m(\mathbf{K}+\mathbf{Q})} \times M_{n\mathbf{K},m\mathbf{K}+\mathbf{Q}}(\mathbf{G})\, M^*_{n\mathbf{K},m\mathbf{K}+\mathbf{Q}}(\mathbf{G}'), \quad (2)$$

where $\Omega = S \times L$ is the normalization volume. In the summation over $\mathbf{K}$, we used $201 \times 201 \times 1$ K-point mesh sampling, which corresponds to the 40 405 Monkhorst-Pack special k points in the Brillouin zone and 6835 in the irreducible Brillouin zone. Band summation (n,m) in (2) is performed over 50 bands and we use the damping parameter $\eta =$ 50 meV. The matrix elements in (2) have the form

$$M_{n\mathbf{K},m\mathbf{K}+\mathbf{Q}}(\mathbf{G}) = \langle \Phi_{n\mathbf{K}} | e^{-i(\mathbf{Q}+\mathbf{G})\mathbf{r}} | \Phi_{n\mathbf{K}+\mathbf{Q}} \rangle_V, \quad (3)$$

where $\mathbf{Q}$ is the momentum transfer vector parallel to the x-y plane, $\mathbf{G} = (\mathbf{G}_\parallel, G_z)$ are 3D reciprocal lattice vectors, and $\mathbf{r} = (\boldsymbol{\rho}, z)$ is a 3D position vector. Integration is performed over the normalization volume V. Plane-wave expansion of the wave function has the form

$$\Phi_{n\mathbf{K}}(\boldsymbol{\rho},z) = \frac{1}{\sqrt{\Omega}} e^{i\mathbf{K}\boldsymbol{\rho}} \sum_{\mathbf{G}} C_{n\mathbf{K}}(\mathbf{G}) e^{i\mathbf{G}\mathbf{r}},$$

where the coefficients $C_{n\mathbf{K}}$ are obtained by solving the LDA-KS equations self-consistently.

The next step is to determine the screened-response function. The free-response function defined as (2) has a 3D character and it is periodic in the direction perpendicular to the q2D crystal plane (z direction), i.e., it is periodically repeated from supercell to supercell, separated by distance L (where one supercell represents one q2D crystal). Therefore, if the screened-response function is calculated by solving the RPA Dyson equation,

$$\chi_{\mathbf{G}\mathbf{G}'}(\mathbf{Q},\omega) = \chi^0_{\mathbf{G}\mathbf{G}'}(\mathbf{Q},\omega) + \sum_{\mathbf{G}_1\mathbf{G}_2} \chi^0_{\mathbf{G}\mathbf{G}_1}(\mathbf{Q},\omega)\, V^{3D}_{\mathbf{G}_1\mathbf{G}_2}(\mathbf{Q})\, \chi_{\mathbf{G}_2\mathbf{G}'}(\mathbf{Q},\omega), \quad (4)$$

where

$$V^{3D}_{\mathbf{G}_1\mathbf{G}_2}(\mathbf{Q}) = \frac{4\pi}{|\mathbf{Q}+\mathbf{G}_1|^2} \delta_{\mathbf{G}_1\mathbf{G}_2} \quad (5)$$

represents the matrix of the bare Coulomb interaction, then it will not represent the polarizability of a single independent q2D crystal because it will contain the effects of interaction with surrounding q2D crystals. However, the interaction with the surrounding supercells can be easily completely eliminated. Instead of performing the complete Fourier transform (5), we can start from the partially Fourier-transformed RPA Dyson equation,

$$\chi_{\mathbf{G}_\parallel\mathbf{G}'_\parallel}(\mathbf{Q},\omega,z,z') = \chi^0_{\mathbf{G}_\parallel\mathbf{G}'_\parallel}(\mathbf{Q},\omega,z,z') + \sum_{\mathbf{G}_{\parallel 1}} \int_{-L/2}^{L/2} dz_1 dz_2 \times \chi^0_{\mathbf{G}_\parallel\mathbf{G}_{\parallel 1}}(\mathbf{Q},\omega,z,z_1)\, v^{2D}_{\mathbf{G}_\parallel 1}(\mathbf{Q},z_1,z_2)\, \chi_{\mathbf{G}_{\parallel 1},\mathbf{G}'_\parallel}(\mathbf{Q},\omega,z_2,z'). \quad (6)$$

Since the z coordinate remains untransformed, the 2D Fourier transform of the bare Coulomb interaction becomes

$$v^{2D}_{\mathbf{G}_\parallel}(\mathbf{Q},z,z') = \frac{2\pi}{|\mathbf{Q}+\mathbf{G}_\parallel|} e^{-|\mathbf{Q}+\mathbf{G}_\parallel||z-z'|}, \quad (7)$$

and

$$\chi^0_{\mathbf{G}_\parallel\mathbf{G}'_\parallel}(\mathbf{Q},\omega,z,z') = \frac{1}{L} \sum_{G_z G'_z} \chi^0_{\mathbf{G}\mathbf{G}'}(\mathbf{Q},\omega) e^{iG_z z - iG'_z z'} \quad (8)$$

represents the Fourier expansion of the independent electron response function in the z and z' directions.

Since the integrations in (6) are performed from $-L/2$ to $L/2$, the interaction between density fluctuations via the Coulomb propagator $v^{2D}_{\mathbf{G}_{\parallel 1}}(\mathbf{Q},z_1,z_2)$ is possible only within the same layer, while the interaction with the polarization in surrounding layers is completely excluded. After inserting the Fourier expansion (8), and a similar one for χ, in the RPA Dyson equation (6) it again becomes a matrix equation,

$$\chi_{\mathbf{G}\mathbf{G}'}(\mathbf{Q},\omega) = \chi^0_{\mathbf{G}\mathbf{G}'}(\mathbf{Q},\omega) + \sum_{\mathbf{G}_1\mathbf{G}_2} \chi^0_{\mathbf{G}\mathbf{G}_1}(\mathbf{Q},\omega)\, V^{2D}_{\mathbf{G}_1\mathbf{G}_2}(\mathbf{Q})\, \chi_{\mathbf{G}_2\mathbf{G}'}(\mathbf{Q},\omega). \quad (9)$$

However, now the matrix of the bare Coulomb interaction becomes

$$V^{2D}_{\mathbf{G}_1\mathbf{G}_2}(\mathbf{Q}) = V^{3D}_{\mathbf{G}_1\mathbf{G}_2}(\mathbf{Q}) - p_{G_{z1}}p_{G_{z2}}\frac{4\pi(1-e^{-|\mathbf{Q}+\mathbf{G}_{\parallel 1}|L})}{|\mathbf{Q}+\mathbf{G}_{\parallel 1}|L} \times \frac{|\mathbf{Q}+\mathbf{G}_{\parallel 1}|^2 - G_{z1}G_{z2}}{\left(|\mathbf{Q}+\mathbf{G}_{\parallel 1}|^2+G^2_{z1}\right)\left(|\mathbf{Q}+\mathbf{G}_{\parallel 1}|^2+G^2_{z2}\right)}\delta_{\mathbf{G}_{\parallel 1}\mathbf{G}_{\parallel 2}}, \tag{10}$$

with

$$p_{G_z} = \begin{cases} 1, & G_z = \frac{2k\pi}{L} \\ -1, & G_z = \frac{(2k+1)\pi}{L}, \end{cases} \qquad k = 0,1,2,3,\ldots.$$

This means that the screened response function of q2D crystals can be obtained the same way as in 3D (bulk) calculation [Eqs. (2)–(5)], with the matrix of the bare Coulomb interaction (5) replaced by (10). This method has already been successfully applied to the calculation of the dynamically screened Coulomb interaction in graphene [27,28,39–41].

The solution of Eq. (5) has the form

$$\chi_{\mathbf{G}\mathbf{G}'}(\mathbf{Q},\omega) = \sum_{\mathbf{G}_1}\mathcal{E}^{-1}_{\mathbf{G}\mathbf{G}_1}(\mathbf{Q},\omega)\chi^0_{\mathbf{G}_1\mathbf{G}'}(\mathbf{Q},\omega), \tag{11}$$

where we have introduced the dielectric matrix

$$\mathcal{E}_{\mathbf{G}\mathbf{G}'}(\mathbf{Q},\omega) = \delta_{\mathbf{G}\mathbf{G}'} - \sum_{\mathbf{G}_1} V^{2D}_{\mathbf{G}\mathbf{G}_1}(\mathbf{Q})\chi^0_{\mathbf{G}_1\mathbf{G}'}(\mathbf{Q},\omega). \tag{12}$$

In the calculation of (11), we neglect the crystal local-field effects in the parallel direction, but not in the perpendicular direction. This approximation is valid only for small values of Q, but fortunately the most interesting features occur in that part of the excitation spectra. Therefore, in all calculations, we set $\mathbf{G}_\parallel = 0$ and we use 20 Hartree (544 eV) as the energy cutoff for the Fourier expansion over G_z's (which corresponds to 61 G_z vectors). This cutoff proved to be sufficient to give a smooth, monotonically decaying, asymptotic behavior of induced charge density for $z > a/2$.

C. Propagator of the dynamically screened Coulomb interaction

The propagator of the induced dynamically screened Coulomb interaction can be calculated from the response function (11) as

$$W^{\text{ind}}_{\mathbf{G}_\parallel}(\mathbf{Q},\omega,z,z') = \int_{-L/2}^{L/2} dz_1 dz_2 v^{2D}_{\mathbf{G}_\parallel}(\mathbf{Q},z,z_1) \times \chi_{\mathbf{G}_\parallel 0}(\mathbf{Q},\omega,z_1,z_2)\, v^{2D}_0(\mathbf{Q},z_2,z'), \tag{13}$$

where the index zero means that $\mathbf{G}'_\parallel = 0$. After using expansion (8) [where independent electron response matrix χ^0 should be replaced by the RPA response matrix (11)] and (7), the integrations over z_1 and z_2 can be performed analytically. Then the induced dynamically screened interaction at $z > a/2$, $z' > a/2$ [i.e., in the region where the profile of electronic density vanishes, as shown in Fig. 2(a)] can be written as

$$W^{\text{ind}}_{\mathbf{G}_\parallel}(\mathbf{Q},\omega,z,z') = e^{-|\mathbf{Q}+\mathbf{G}_\parallel|z-Qz'}D_{\mathbf{G}_\parallel}(\mathbf{Q},\omega), \tag{14}$$

where we introduced the propagator of surface excitations,

$$D_{\mathbf{G}_\parallel}(\mathbf{Q},\omega) = \sum_{G_{z1}G_{z2}} \chi_{\mathbf{G}_\parallel,0,G_{z1},G_{z2}}(\mathbf{Q},\omega)F_{G_{z1}}(\mathbf{Q}+\mathbf{G}_\parallel)F^*_{G_{z2}}(\mathbf{Q}). \tag{15}$$

Here the form factors F are

$$F_{G_z}(\mathbf{Q}) = \frac{4\pi p_{G_z}}{Q\sqrt{L}}\,\frac{sh\left(\frac{QL}{2}\right)}{Q+iG_z}. \tag{16}$$

The imaginary part of the induced potential (14) can be used to calculate the energy dissipation rate of a dynamical external perturbation. For example, if the external perturbation is a static point charge placed at $z_0 > a/2$ and oscillating as $\rho(\mathbf{r},t) = \delta(\mathbf{r}-\mathbf{r}_0)\cos(\omega t)$ [39], then the $\mathbf{Q}$ Fourier component of its energy dissipation rate is proportional to the imaginary part of the induced potential (14). Generally, the $\mathbf{Q}$ Fourier component of the external perturbation can excite electronic modes with wave vectors $\mathbf{Q}+\mathbf{G}$, where $\mathbf{G}$ can be any reciprocal lattice vector. This means that each $\mathbf{Q}$ component simultaneously loses energy to the sum of all $\mathbf{Q}+\mathbf{G}$ modes. However, the energy transfer is most intense to the excitation of $\mathbf{Q}+\mathbf{G}$ mode with $\mathbf{G}_\parallel = 0$. This means that the spectral function, which defines the intensity of energy loss by an external perturbation to excitation of $(\mathbf{Q},\omega)$ modes, can be written as

$$S(\mathbf{Q},\omega) = -\text{Im}D_{\mathbf{G}_\parallel=0}(\mathbf{Q},\omega). \tag{17}$$

The induced potential can be written as

$$W^{\text{ind}}(\mathbf{Q},\omega,z,z') = D_{\mathbf{G}_\parallel=0}(\mathbf{Q},\omega)e^{-Q(z+z')}. \tag{18}$$

D. Model dielectric functions

Considering the atomic thickness of q2D crystals, the first attempt to derive its dielectric response is to consider it as intrinsically two dimensional. Connection between the 3D response function (2) and the corresponding 2D response function (obtained by reducing the 3D response function to the $z = 0$ plane) is simply given by

$$\chi^0_{2D}(\mathbf{Q},\omega) = L\chi^0_{\mathbf{G}=0,\mathbf{G}'=0}(\mathbf{Q},\omega). \tag{19}$$

The 2D dielectric function is then

$$\varepsilon_{2D}(\mathbf{Q},\omega) = 1 - v_Q\chi^0_{2D}(\mathbf{Q},\omega), \tag{20}$$

where $v_Q = \frac{2\pi}{Q}$. The ϵ_{2D} describes the dielectric response of the MoS_2-ML which has been forced to be an intrinsically 2D system. Therefore, in the long-wavelength limit ($Q \ll 1/a$), this model dielectric function is able to provide good 2D screening. In other words, in this case for example, v_Q/ϵ_{2D} can be considered as the 2D Fourier transform of the screened Coulomb interaction in the $z = 0$ plane, i.e., the plane to which the MoS_2-ML is reduced. Since the tight-binding approach (TBA) usually treats q2D crystals as purely two-dimensional systems (e.g., effective two-band TBA model developed in Ref. [31] and applied to MoS_2-ML), it is useful to compare the TBA and the *ab initio* 2D dielectric function obtained using the density functional theory (DFT) approach. For example, the TBA model provides much more refined structures in the dielectric function which helps in the analysis of the DFT 2D

dielectric function. Here we briefly describe the derivation of the dielectric function in the spirit of the effective TBA model.

In order to obtain the TBA-2D response function (19) [similar as for the DFT 3D density-density response function (2)], we need the TBA band structure $E_n(\mathbf{K})$ and the charge vertices $M_{n\mathbf{K},m\mathbf{K+Q}}$. The calculation of the band structure in the effective two-band TBA model is described in Ref. [31], and the charge vertices can be extracted from the current vertices. The interaction Hamiltonian and the corresponding current vertices are defined in Ref. [31] with the aide of Peierls substitution, and here we briefly present the connection between the charge and current vertices.

The μth Cartesian component of the current operator is defined as

$$\hat{J}_\mu(\mathbf{Q}) = \sum_{nm}\sum_{\mathbf{K}} J^\mu_{n\mathbf{K},m\mathbf{K+Q}} c^\dagger_{n\mathbf{K}} c_{m\mathbf{K+Q}}, \tag{21}$$

where the current vertices $J^\mu_{n\mathbf{K},m\mathbf{K+Q}}$ are calculated in Ref. [31]. The charge vertices can be express in terms of the current vertices by using the continuity equation and the Heisenberg equation,

$$i\,Q_\mu \hat{J}_\mu(\mathbf{Q}) = i\hbar \frac{\partial \hat{\rho}(\mathbf{Q})}{\partial t} = [\hat{\rho}(\mathbf{Q}), \hat{H}_0], \tag{22}$$

where the density operator in the two-band model representation is

$$\hat{\rho}(\mathbf{Q}) = \sum_{nm}\sum_{\mathbf{K}\sigma} M_{n\mathbf{K},m\mathbf{K+Q}} c^\dagger_{n\mathbf{K}\sigma} c_{m\mathbf{K+Q}\sigma}. \tag{23}$$

In (22), we have used the bare electron Hamiltonian,

$$\hat{H}_0 = \sum_{n\mathbf{K}\sigma} E_n(\mathbf{K}) c^\dagger_{n\mathbf{K}\sigma} c_{n\mathbf{K}\sigma}. \tag{24}$$

After using (22)–(24) and performing the commutation relations, it is easy to obtain the connection between the charge and current vertices,

$$M_{n\mathbf{K},m\mathbf{K+Q}} = \frac{Q_\mu J^\mu_{n\mathbf{K},m\mathbf{K+Q}}}{E_m(\mathbf{K+Q}) - E_n(\mathbf{K})}. \tag{25}$$

After inserting (25) in (19), we finally obtain the 2D response function and the corresponding 2D dielectric function (20). From the DFT point of view, the most frequently used model dielectric function is the macroscopic dielectric function, which can be obtained directly from the dielectric matrix (12) as

$$\epsilon_M(\omega) = 1/\mathcal{E}^{-1}_{\mathbf{G}=0\mathbf{G}'=0}(\mathbf{Q}\to 0,\omega). \tag{26}$$

Assuming that in the long-wavelength limit the crystal local-field effects become negligible, we can keep only $\mathbf{G} = \mathbf{G}' = 0$ components and the Coulomb interaction matrix (10) becomes

$$\lim_{Q\to 0} V^{2D}_{G=0G'=0}(Q) = \frac{2\pi L}{Q}.$$

Moreover, after combining it with definitions (12), (19), (20), and (26), one can easily show that

$$\lim_{Q\to 0} \varepsilon_{2D}(\mathbf{Q},\omega) = \epsilon_M(\omega). \tag{27}$$

Therefore, the ϵ_M, like the ϵ_{2D}, describes the dielectric response of the "two-dimensional" MoS_2-ML in the long-wavelength limit. In other words, these dielectric functions cannot be used if MoS_2 is considered to be a dielectric slab of finite thickness a. In that case, it would probably be better to calculate the "bulk" macroscopic dielectric function ϵ_M of the three-dimensional MoS_2 crystal [in which case we would insert the Coulomb interaction matrix (5) and response function (2) for the 3D crystal into (12)], which would correspond to some effective dielectric function of the MoS_2 dielectric slab. However, this 3D macroscopic dielectric function is still not suitable for the description of a microscopically thin MoS_2-ML because in that case the effective dielectric function is still heavily influenced by the MoS_2 "slab" boundaries.

In order to examine the response of the MoS_2-ML to an external homogeneous electrical field, it is more convenient to use the dielectric tensor or the transversal dielectric function [32,42,43],

$$\epsilon_{\mu\nu}(\omega) = \delta_{\mu\nu} + \frac{4\pi c}{\omega^2}\Pi^0_{\mu\nu}(\mathbf{Q}=0,\omega). \tag{28}$$

The current-current response tensor $\Pi^0_{\mu\nu,\mathbf{GG}'}$ in the long-wavelength limit $\mathbf{Q}\approx 0$ can be written as [32]

$$\Pi^0_{\mu\nu}(\mathbf{Q},\omega) = \Pi^{0,\mathrm{intra}}_{\mu\nu}(\mathbf{Q},\omega) + \Pi^{0,\mathrm{inter}}_{\mu\nu}(\mathbf{Q},\omega), \tag{29}$$

where the intraband contribution is [44–46]

$$\Pi^{0,\mathrm{intra}}_{\mu\nu}(\omega,\mathbf{Q}\approx 0) = \frac{n_{\mu\nu}}{c}\frac{\hbar\omega}{\hbar\omega + i\,\eta_{\mathrm{intra}}}, \tag{30}$$

and where

$$n_{\mu\nu} = \frac{2}{\Omega}\sum_{\mathbf{K},n}\frac{\partial f(E_{n\mathbf{K}})}{\partial E_{n\mathbf{K}}} j^\mu_{n\mathbf{K},n\mathbf{K}}(\mathbf{G}=0)\,[j^\nu_{n\mathbf{K},n\mathbf{K}}(\mathbf{G}'=0)]^* \tag{31}$$

represents the effective number of charge carriers. The interband term is

$$\begin{aligned}\Pi^{0,\mathrm{inter}}_{\mu\nu}(\omega,\mathbf{Q}\approx 0) = \frac{2}{\Omega c}\sum_{\mathbf{K},n\neq m}&\frac{\hbar\omega}{E_{n\mathbf{K}} - E_{m\mathbf{K}}}\\ &\times\frac{f_{n\mathbf{K}} - f_{m\mathbf{K}}}{\hbar\omega + i\,\eta_{\mathrm{inter}} + E_{n\mathbf{K}} - E_{m\mathbf{K}}}\\ &\times J^\mu_{n\mathbf{K},m\mathbf{K}}(\mathbf{G}=0)\,[J^\nu_{n\mathbf{K},m\mathbf{K}}(\mathbf{G}'=0)]^*.\end{aligned} \tag{32}$$

The calculation of the current vertices $J^\mu_{n\mathbf{K},m\mathbf{K}}(\mathbf{G})$ is described in detail in Ref. [32]. Using the dielectric tensor (28), we can decompose the dielectric function in parallel x-y and z directions and investigate the dielectric response in these directions separately, so we introduce the notation

$$\epsilon_\parallel(\omega) = \epsilon_{xx}(\omega),\ \ \epsilon_\perp(\omega) = \epsilon_{zz}(\omega). \tag{33}$$

Another way to determine the effective dielectric function of q2D is to follow the methodology used in spectroscopic ellipsometry experiments [22,47], where the dielectric function is extracted from the reflectivity coefficient calculated by treating the q2D as a classical dielectric slab. Here we use a similar method, but in the nonretarded $c\to 0$ (electrostatic) limit. We assume that the MoS_2 monolayer is a dielectric slab with thickness a and dielectric function $\epsilon_{\mathrm{eff}}(\omega)$, as sketched in Fig. 2(b). After solving the Poisson equation for the point charge placed in region $z' > a/2$, and applying the boundary condition, we determine the induced potential at

point $z > a/2$,

$$W_{cl}^{\text{ind}}(\mathbf{Q},\omega,z,z') = D_{cl}(\mathbf{Q},\omega)e^{-Q(z+z')}, \tag{34}$$

where

$$D_{cl}(\mathbf{Q},\omega) = v_Q D_S(\omega)\frac{e^{Qa} - e^{-Qa}}{1 - [D_S(\omega)]^2 e^{-2Qa}}, \tag{35}$$

and where $D_S(\omega) = [1 - \epsilon_{\text{eff}}(\omega)]/[1 + \epsilon_{\text{eff}}(\omega)]$. By equating classical induced potential (34) and induced potential (18) (calculated from the first principles), i.e., $D_{cl} = D_{\mathbf{G}_\parallel=0}$, we can extract the effective dielectric function of the MoS_2 monolayer $\epsilon_{\text{eff}}(\omega)$.

III. RESULTS

A. Spectra of electronic excitations in MoS_2-ML

Figure 4 shows the spectra of electronic excitations in MoS_2-ML, i.e., the Q Fourier component of the energy-loss rate of a blinking point charge placed at $z = a/2$ near MoS_2-ML, as a function of the blinking frequency ω, obtained from (17). This quantity can be compared with EELS measurements.

The origin of particular peaks in the optical absorption spectra is explained in detail in Ref. [31], and here we examine the response to a longitudinal external perturbation at finite wave vector Q, which leads to slightly different features in the spectra. The characteristic peaks in the spectra are marked by letters $A, B, \ldots, G$, and the corresponding electron-hole transitions are marked by the same letters in the band structure and the DOS shown in Fig. 3. Usually, the term valence band is used for the highest occupied band, while the term conductance band is used for the lowest unoccupied band, but here we extend that terminology to a few more bands, denoting them by numbers based on their distance from the Fermi level. In other words, the lowest unoccupied band is called the first conductance band, the one above it is called the second conductance band, etc., while the highest occupied band is called the first valence band, the one below it is called the second valence band, etc. The main contribution to the energy-loss rate comes from the transitions between the first

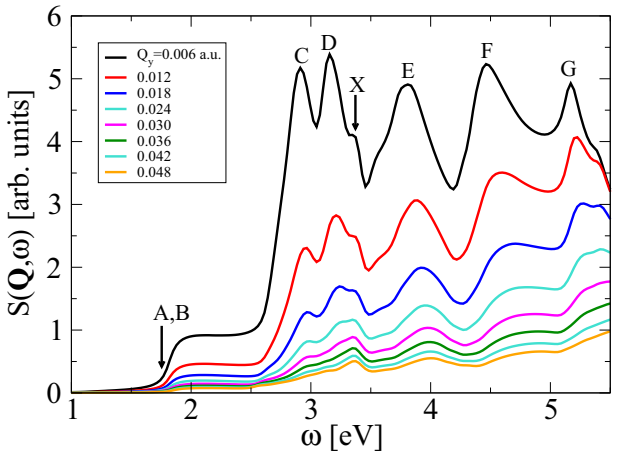

FIG. 4. Spectra of electronic excitations in MoS_2-ML obtained from (17).

two valence bands and the first two conduction bands, which are almost completely composed of Mo(d) and S(p) orbitals, as shown in Ref. [31].

The excitation spectra first show an onset (denoted as A, B) at about 1.75 eV and a slowly increasing plateau corresponding to Mo(d)↔ S(p) excitations around the K point. The letters A and B are reserved for two spin-orbit (SO) split excitons [4,5,48–50], which do not appear here due to the fact that we are using RPA which excludes excitonic effects. The first intensive peak at 2.9 eV, denoted as C, corresponds to Mo(d)↔ S(p) excitations between the states in the vicinity of the H point and the states in the vicinity of P points, which are both saddle points, i.e., the van Hove singularities manifested as sharp peaks in DOS (Fig. 3). The peak at 3.15 eV, denoted as D, corresponds to the transitions between van Hove singularities in valence and conducting bands around the M point, which are also manifested as intensive peaks in DOS. In addition to the high density of states, valence and conducting bands at the M point also exhibit predominant (∼80%) S(p) and (∼80%) M(d) characters, respectively [31], which further increases the intensity of the transitions between them. The third, small maximum at 3.4 eV, denoted as X, originates from the transitions between parallel (holelike) parabolic bands around the Γ point. This is intriguing because this peak also appears as a very intensive peak in the joint density of states (JDOS) [31]. However, there are no van Hove singularities in the DOS in Fig. 3 from which it would originate. If we look at the expression for the two-dimensional DOS [51], even at the top of the parabolic bands $\nabla_{\mathbf{K}} E_n(\mathbf{K}) = 0$, it does not necessarily mean that there is a singularity in the DOS. The best example is the density of state of the 2D free-electron gas. Even though the dispersion is parabolic $E(\mathbf{K}) = \frac{\hbar^2\mathbf{K}^2}{2m}$, the DOS is step function $\text{DOS}(E) \sim \theta(E)$ which is not singular. This step, which originates from the first valence parabolic band around the Γ point, can also be observed in the DOS of MoS_2-ML, as indicated by the red arrow in Fig. 3. The points in the band structure responsible for the singularities in the two-dimensional DOS are the saddle points (e.g., points H and P in the band structure in Fig. 3), and the hyperbolic points which occur in almost any band around the M point of the MoS_2-ML band structure in Fig. 3. Therefore, the JDOS is intense, not because of the high DOS of parabolic bands but because the JDOS depends on the energy difference, and there are many equally separated energy levels lying on the "parallel" parabolas in the Γ point. Moreover, the X peak in the excitation spectra is highly reduced, probably due to the matrix elements (3) that are not present in JDOS. The peak at 3.8 eV, denoted as E, is a result of the transitions between the van Hove singularities in the second valence band and the second conduction band at the M point. The peak at 4.5 eV denoted by F and the peak at 5.2 eV denoted by G are the results of transitions which again occur in the vicinity of the M point. This time the transitions are from the third valence to second conductance band (transition F in Fig. 3) and from the first valence to the fourth conductance band (transition G in Fig. 3). The third valence and fourth conductance bands exhibit strong van Hove singularities in the M point, as denoted by F and G in DOS of Fig. 3. The peaks $A = 2.9$ eV, $B = 3.8$ eV, $C = 4.5$ eV, and $D = 5.5$ eV reported in Ref. [24] are in very nice agreement with our peaks $C = 2.9$ eV, $E = 3.8$ eV,

$F = 4.5$ eV, and $G = 5.2$ eV, respectively, while the absence of peaks X and D is probably due to lower resolution of their calculations.

We can see that the spectral weight of all electronic excitations rapidly decreases with the transfer wave vector Q. The same trend is noticed in the EELS experiment [29], and also in Ref. [31] where the absorption spectrum rapidly decreases as incident electromagnetic field angle θ (or parallel wave vector Q) increases. This means that MoS_2 is completely transparent for the grazing incidence light. This behavior is attributed to the fact that all charge density modes (within the shown frequency interval) have in-plane character and are located in the molybdenum plane. The EELS experiment [29] shows a group of strong transitions centered at $\alpha = 3.1$ eV, a sharp but weak peak at $\delta = 3.9$ eV, and a broad peak at $\beta = 4.5$ eV, which agrees well with our peaks $C = 2.9$ eV, $E = 3.8$ eV, and $F = 4.5$ eV, respectively.

B. Dielectric function in MoS_2-ML

As we already showed in Sec. II D, the definition of the dielectric function in q2D materials is not unique. We introduced the 2D dielectric function $\epsilon_{2D}(\omega)$ which is the 3D nonlocal dielectric function averaged over z and z' and reduced to the $z = 0$ plane, as well as the so-called "macroscopic dielectric function" $\epsilon_M(\omega)$ obtained by the matrix inversion (26) of the 3D nonlocal dielectric function. Another definition arises from studying the response (polarization **P**) of q2D immersed into the external homogeneous electrical field **E** (gate voltage). Because of strong anisotropy, the response depends on the direction of the applied electric field, which provides division to the parallel (x-y plane) $\epsilon_\parallel(\omega)$ and perpendicular (z direction) $\epsilon_\perp(\omega)$ dielectric functions. Finally, we can define the dielectric function by analyzing the reflected (or transmitted) electromagnetic field incident to q2D, which is considered as a dielectric slab (with sharp boundaries) described by some local effective dielectric function $\epsilon_{\text{eff}}(\omega)$. Here we present these dielectric functions, and compare them with each other and with available experimental results.

The black solid lines in Fig. 5 show the *ab initio* DFT result for the real (upper panel) and imaginary (lower panel) parts of the two-dimensional dielectric function obtained from Eq. (20). The transfer wave vector is $Q = 0.006$ a.u. and it is chosen to be in the Γ-M direction of the first Brillouin zone. For comparison, blue dashed lines show the same dielectric function obtained in the TBA model. We can see that the TBA provides more intensive and refined structures than the full numerical *ab initio* calculations. This is because the TBA dielectric function is calculated using the charge vertices (25) and energies $E_n(\mathbf{K})$, which are calculated analytically, including only two bands in the calculation. The TBA parameters are adjusted to achieve the best agreement between the TBA and the *ab initio* DFT band structures. However, since the same parameters define the charge vertices (25), the TBA spectral intensities do not necessarily agree with the DFT spectral intensities. Moreover, since we want to emphasize the appearance of certain structures in the spectrum, we decreased the damping constant in the TBA calculation to $\eta = 10$ meV, which additionally sharpened the structures in the TBA dielectric function.

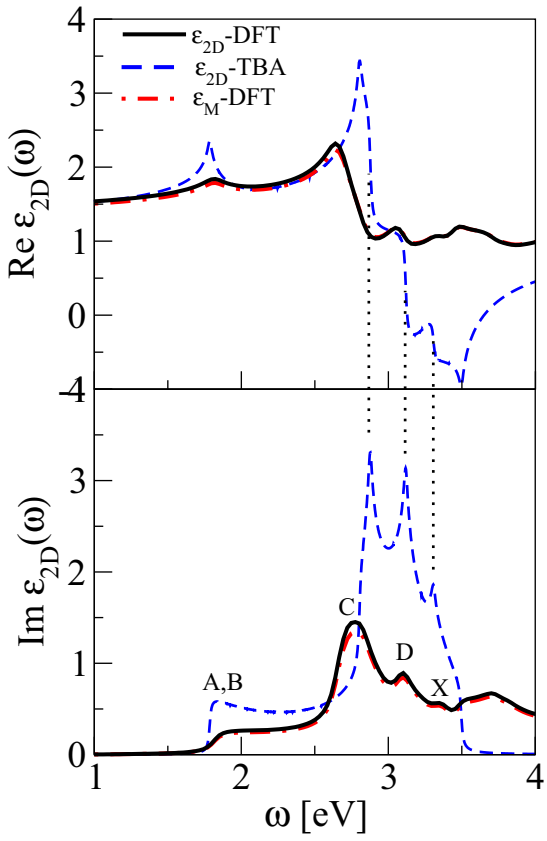

FIG. 5. Two-dimensional dielectric function $\epsilon_{2D}(\mathbf{Q},\omega)$ given by Eq. (20) obtained using the *ab initio* method (black solid line) and by using the TBA model (blue dashed line). Macroscopic dielectric function $\epsilon_M(\omega)$ given by Eq. (26) (red dash-dotted line) is also shown for comparison. The transfer wave vector is $Q = 0.006$ a.u. and is chosen to be in Γ-M direction of the first Brillouin zone.

As in the case of excitation spectra, the imaginary part of the DFT dielectric function shows excitation onset at about 1.7 eV (denoted by A, B), where the real part first exhibits the small peak. At about 2.9 eV, the imaginary part shows a strong peak and the real part drops down, which confirms the high density of Mo(d)↔ S(p) excitations in that region. Peaks D (3.15 eV) and X (3.4 eV), already discussed in the excitation spectra, are also visible. The TBA results show even more pronounced (sharper) structures. For example, the imaginary part of the TBA dielectric function shows very sharp and intense peaks C, D, and X. Moreover, they are very accurately followed by corresponding drops in the real part of the dielectric function (denoted by black dotted lines), which nicely confirms the nature of the excitation spectra discussed in Sec. III A. The red dash-dotted lines in Fig. 5 show the results for the real and imaginary parts of the macroscopic dielectric function obtained from Eq. (26). It is clear that ϵ_{2D} exactly coincides with ϵ_M. Considering the derivation of the Eq. (27), this implies that the crystal local-field effects or dispersivity of the dielectric response in the z direction (direction of high anisotropy) are completely irrelevant in the long-wavelength limit.

The black solid line in Fig. 6 shows the real and imaginary parts of the effective dielectric function in MoS_2-ML

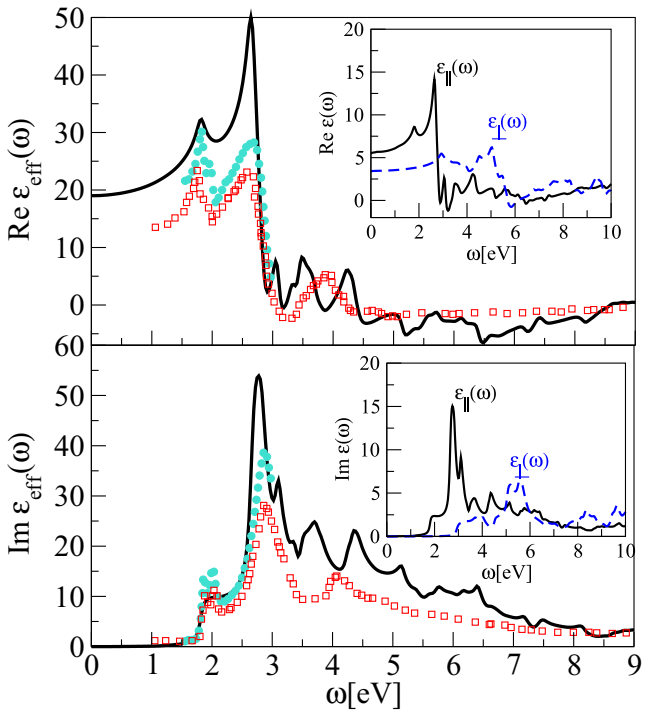

FIG. 6. Dielectric function in MoS_2-ML calculated from $D = D_{\mathbf{G}_\parallel=0}$ (black solid line); experimental dielectric function taken from Ref. [21] (turquoise dots) and from Ref. [22] (red squares). Insets show parallel $\epsilon_\parallel(\omega)$ (black solid line) and perpendicular $\epsilon_\perp(\omega)$ (blue dashed line) dielectric functions calculated from dielectric tensor (28)–(33).

calculated by equating induced (or reflected) potentials (34) and (18), i.e., from $D_{cl} = D_{\mathbf{G}_\parallel=0}$. We compare the dielectric function constructed this way with the dielectric function extracted from ellipsometry measurements taken from Ref. [21] (turquoise dots) and from Ref. [22] (red squares). Taking into account the fact that our RPA result does not include the excitonic effects, the agreement with experimental dielectric functions is satisfactory. Also, our results in the infrared (IR) and visible frequency range show good quantitative agreement with the dielectric functions extracted from optical measurements reported in Refs. [52–54].

The insets in Fig. 6 show the imaginary and real parts of the parallel $\epsilon_\parallel(\omega)$ (black solid line) and perpendicular $\epsilon_\perp(\omega)$ (blue dashed line) dielectric function, calculated using definitions (28)–(33). Very similar results have already been theoretically obtained [24]. Even though the features appearing in $\epsilon_\parallel(\omega)$ are qualitatively very similar to those appearing in $\epsilon_{\text{eff}}(\omega)$, it is clear that the results shown in the insets are not quantitatively comparable with the dielectric function extracted from optical measurements. For example, the experimental and theoretical values of the effective dielectric function ϵ_{eff} in the IR frequency range ($\omega \approx 1$ eV) are 15 and 20, respectively, while the value of $\epsilon_\parallel$ in the same frequency range is 6, which is about three times smaller. This is reasonable because in the first method the q2D crystal is considered as a dielectric slab described by $\epsilon_{\text{eff}}(\omega)$ from which the electromagnetic field reflects, while the second case represents the realistic response to an homogeneous electric field. It can also be seen that the 2D and macroscopic dielectric functions, presented in Fig. 5, are an order of magnitude smaller than the effective and parallel dielectric functions. This suggests that dielectric functions ϵ_{2D} and ϵ_M are not suitable for the description of the q2D response. However, the ϵ_{2D} and ϵ_M provide a good screened Coulomb interaction in q2D considered as intrinsically 2D crystals, in the long-wavelength limit ($Q \ll 1/a$). Moreover, it is safe to assume that the ϵ_{eff} first rapidly changes with thickness (when the thickness is still several MoS_2 MLs), until it saturates in the 3D macroscopic dielectric function for larger (macroscopic) thicknesses. Most likely this is the reason why the ϵ_{2D} or ϵ_M are quantitatively so different from the ϵ_{eff}, where the MoS_2-ML is treated neither as a macroscopic slab cut from the bulk crystal nor as a 2D material.

TABLE I. Comparison of static dielectric constants in MoS_2-ML with other theoretical and experimental results.

	$\epsilon_\parallel(0)$	$\epsilon_\perp(0)$
This work	5.5	3.4
Ref. [24]	4.8,	3.0
Ref. [25]	7.36	1.6
Ref. [26]	4.2	2.8
Ref. [23] (expt.)	4.0	

The static values of the dielectric functions $\epsilon_\parallel(\omega = 0)$ and $\epsilon_\perp(\omega = 0)$ listed in Table I are calculated using the dielectric tensor [Eqs. (28)–(33)]. We can see that our $\epsilon_\parallel(0) = 5.5$ is in good agreement with the experimental value of 4.0 [23] measured within the study of a thickness-dependent static dielectric constant in MoS_2. Since it is possible that the electric field applied in these measurements was not completely parallel to the MoS_2-ML plane, there is a possibility for the occurrence of small $\epsilon_\perp$ admixture, which would reduce the measured value of $\epsilon_\parallel$. The accuracy of the calculation of the statical longitudinal dielectric function $\epsilon_\parallel(0)$ can be significantly affected by the accuracy of the calculation of the isothermal response related to the intraband transitions, as investigated in Refs. [55,56]. Here, in the calculation of the dielectric tensor, we use the current-current response tensor (29) which includes both the intraband and the interband transitions. However, the derivative of the Fermi-Dirac distribution in (31) can, even up to the room temperatures $T \approx 300$ K, be considered as a very narrow Lorentzian (in comparison with MoS_2-ML band gap) which is, for semiconductors such as MoS_2-ML, placed in the band gap. Therefore, the effective number of charge carriers (31) is almost exactly zero, and the contribution of the intraband term (30) to the $\epsilon_\parallel(\omega)$ is negligible, even in the statistical ($\omega = 0$) limit. Some previous theoretical papers [24–26] also report very good agreement with the measured value of $\epsilon_\parallel$.

IV. CONCLUSIONS

The spectra of electronic excitations in MoS_2-ML is studied and brought in connection with very recent EELS measurements. The particular features in the spectra are associated with the corresponding transitions in the band structure, which is shown to be in accordance with the other calculations and

measurements. The peaks in the visible frequency range are composed of transitions between the valence and conducting Mo(d) and S(p) bands in the region between the Γ and K point, and at the M point of the Brillouin zone. It is shown that the intensity of electronic excitations rapidly decreases with transfer wave vector Q, which is attributed to the fact that the excited charge density oscillations are mostly localized in the Mo plane, as predicted in previous theoretical work. The various model dielectric functions of the MoS_2-ML are studied and compared with previous experiments and theory. It is shown that the widely used 2D dielectric function $\epsilon_{2D}(\omega)$ and macroscopic dielectric functions $\epsilon_M(\omega)$ are totally inadequate to describe dielectric response (polarizability) of q2D crystals. However, they provide good results for the screened Coulomb interaction in q2D considered as intrinsically 2D crystals, in the long-wavelength limit ($Q \ll 1/a$). On the other hand, it is shown that the effective dielectric function $\epsilon_{\text{eff}}(\omega)$ is an appropriate tool for investigation of the interaction of q2D crystals with an external electromagnetic field, while the dielectric functions $\epsilon_{\parallel}$ and $\epsilon_{\perp}$ are very useful for investigation of the response of q2D crystals to an external homogeneous electrical field (gate voltage).

ACKNOWLEDGMENTS

The authors thank I. Kupčić for useful discussions and invaluable advice. Computational resources were provided by the Donostia International Physic Center (DIPC) computing center. V.D. acknowledges support from the QuantiXLie Center of Excellence.

[1] S. Z. Butler, S. M. Hollen, L. Cao, Y. Cui, J. A. Gupta, H. R. Gutirrez, T. F. Heinz, S. S. Hong, J. Huang, A. F. Ismach, E. Johnston-Halperin, M. Kuno, V. V. Plashnitsa, R. D. Robinson, R. S. Ruoff, S. Salahuddin, J. Shan, L. Shi, M. G. Spencer, M. Terrones, W. Windl, and J. E. Goldberger, ACS Nano **7**, 2898 (2013).

[2] Q. H. Wang, K. Kalantar-Zadeh, A. Kis, J. N. Coleman, and M. S. Strano, Nat. Nanotechnol. **7**, 699 (2012).

[3] X. Xu, W. Yao, D. Xiao, and T. F. Heinz, Nat. Phys. **10**, 343 (2014).

[4] A. Splendiani, L. Sun, Y. Zhang, T. Li, J. Kim, C. Y. Chim, G. Galli, and F. Wang, Nano Lett. **10**, 1271 (2010).

[5] K. F. Mak, C. Lee, J. Hone, J. Shan, and T. F. Heinz, Phys. Rev. Lett. **105**, 136805 (2010).

[6] G. Cassabois, P. Valvin, and B. Gil, Nat. Photon. **10**, 262 (2016).

[7] J. S. Lauret, R. Arenal, F. Ducastelle, A. Loiseau, M. Cau, B. Attal-Tretout, E. Rosencher, and L. Goux-Capes, Phys. Rev. Lett **94**, 037405 (2005).

[8] Yong-Nian Xu and W. Y. Ching, Phys. Rev. B **44**, 7787 (1991).

[9] A. K. Geim and I. V. Grigorieva, Nature (London) **499**, 419 (2013).

[10] Wu Hua-Qiang, Linghu Chang-Yang, Lu Hong-Ming, and Qian He, Chin. Phys. B **22**, 098106 (2013).

[11] F. Bonaccorso, Z. Sun, T. Hasan, and A. C. Ferrari, Nat. Photon. **4**, 611 (2010).

[12] A. Pospischil, M. M. Furchi, and T. Mueller, Nat. Nanotechnol. **9**, 257 (2014).

[13] L. Britnell, R. M. Ribeiro, A. Eckmann, R. Jalil, B. D. Belle, A. Mishchenko, Y. J. Kim, R. V. Gorbachev, T. Georgiou, S. V. Morozov, A. N. Grigorenko, A. K. Geim, C. Casiraghi, A. H. C. Neto, and K. S. Novoselov, Science **340**, 1311 (2013).

[14] J. S. Ross, P. Klement, A. M. Jones, N. J. Ghimire, J. Yan, D. G. Mandrus, T. Taniguchi, K. Watanabe, K. Kitamura, W. Yao, D. H. Cobden, and X. Xu, Nat. Nanotechnol. **9**, 268 (2014).

[15] F. H. L. Koppens, T. Mueller, P. Avouris, A. C. Ferrari, M. S. Vitiello, and M. Polini, Nat. Nanotechnol. **9**, 780 (2014).

[16] S. Jo, N. Ubrig, H. Berger, A. B. Kuzmenko, and A. F. Morpurgo, Nano Lett. **14**, 2019 (2014).

[17] O. Lopez-Sanchez, E. Alarcon Llado, V. Koman, A. Fontcuberta i Morral, A. Radenovic, and A. Kis, ACS Nano **8**, 3042 (2014).

[18] C.-H. Lee, G.-H. Lee, A. M. van der Zande, W. Chen, Y. Li, M. Han, X. Cui, G. Arefe, C. Nuckolls, T. F. Heinz, J. Guo, J. Hone, and P. Kim, Nat. Nanotechnol. **9**, 676 (2014).

[19] B. W. H. Baugher, H. O. H. Churchill, Y. Yang, and P. Jarillo-Herrero, Nat. Nanotechnol. **9**, 262 (2014).

[20] M. Bernardi, M. Palummo, and J. C. Grossman, Nano Lett. **13**, 3664 (2013).

[21] Y. Li, A. Chernikov, X. Zhang, A. Rigosi, H. M. Hill, A. M. van der Zande, D. A. Chenet, En-Min Shih, J. Hone, and T. F. Heinz, Phys. Rev. B **90**, 205422 (2014).

[22] W. Li, A. G. Birdwell, Matin Amani, Robert A. Burke, Xi Ling, Yi-Hsien Lee, Xuelei Liang, Lianmao Peng, Curt A. Richter, Jing Kong, David J. Gundlach, and N. V. Nguyen, Phys. Rev. B **90**, 195434 (2014).

[23] Xiaolong Chen, Zefei Wu, Shuigang Xu, Lin Wang, Rui Huang, Yu Han, Weiguang Ye, Wei Xiong, Tianyi Han, Gen Long, Yang Wang, Yuheng He, Yuan Cai, Ping Sheng, and Ning Wang, Nat. Commun. **6**, 6088 (2015).

[24] A. Kumar and P. K. Ahluwalia, Mater. Chem. Phys. **135**, 755 (2012).

[25] A. Molina-Sanchez and L. Wirtz, Phys. Rev. B **84**, 155413 (2011).

[26] T. Cheiwchanchamnangij and Walter R. L. Lambrecht, Phys. Rev. B **85**, 205302 (2012).

[27] V. Despoja, D. J. Mowbray, D. Vlahović, and L. Marušić, Phys. Rev. B **86**, 195429 (2012).

[28] V. Despoja, D. Novko, K. Dekanić, M. Šunjić, and L. Marušić, Phys. Rev. B **87**, 075447 (2013).

[29] J. Hong, Kun Li, Chuanhong Jin, X. Zhang, Ze Zhang, and Jun Yuan, Phys. Rev. B **93**, 075440 (2016).

[30] S. Baroni and R. Resta, Phys. Rev. B **33**, 7017 (1986).

[31] Z. Rukelj, A. Štrkalj, and V. Despoja, Phys. Rev. B **94**, 115428 (2016).

[32] D. Novko, M. Šunjić, and V. Despoja, Phys. Rev. B **93**, 125413 (2016).

[33] P. Giannozzi, S. Baroni, N. Bonini, M. Calandra, R. Car, C. Cavazzoni, D. Ceresoli, G. L. Chiarotti, M. Cococcioni, I. Dabo *et al.*, J. Phys.: Condens. Matter **21**, 395502 (2009).

[34] C. Hartwigsen, S. Goedecker, and J. Hutter, Phys. Rev. B **58**, 3641 (1998); S. Goedecker, M. Teter, and J. Hutter, **54**, 1703 (1996).

[35] J. P. Perdew and A. Zunger, Phys. Rev. B **23**, 5048 (1981).
[36] T. Cao, G. Wang, W. Han, H. Ye, C. Zhu, J. Shi, Q. Niu, P. Tan, E. Wang, B. Liu, and J. Feng, Nat. Commun. **3**, 887 (2012).
[37] H. J. Monkhorst and J. D. Pack, Phys. Rev. B **13**, 5188 (1976).
[38] L. Hedin, Phys. Rev. **139**, A796 (1965); G. Strinati, Phys. Rev. B **29**, 5718 (1984).
[39] V. Despoja, K. Dekanić, M. Šunjić, and L. Marušić, Phys. Rev. B **86**, 165419 (2012).
[40] V. Despoja and M. Šunjić, Phys. Rev. B **88**, 245416 (2013).
[41] D. Novko, V. Despoja, and M. Šunjić, Phys. Rev. B **91**, 195407 (2015).
[42] V. Despoja, M. Šunjić, and L. Marušić, Phys. Rev. B **80**, 075410 (2009).
[43] V. Despoja, M. Šunjić, and L. Marušić, Phys. Rev. B **83**, 165421 (2011).
[44] I. Kupčić, Phys. Rev. B **90**, 205426 (2014).
[45] I. Kupčić, Phys. Rev. B **91**, 205428 (2015).
[46] I. Kupčić, Physica B **322**, 154 (2002).
[47] Chanyoung Yim, Maria O'Brien, Niall McEvoy, Sinead Winters, Inam Mirza, James G. Lunney, and Georg S. Duesberg, Appl. Phys. Lett. **104**, 103114 (2014).
[48] Diana Y. Qiu, F. H. da Jornada, and S. G. Louie, Phys. Rev. Lett. **111**, 216805 (2013).
[49] A. Molina-Sanchez, D. Sangalli, K. Hummer, A. Marini, and L. Wirtz, Phys. Rev. B **88**, 045412 (2013).
[50] K. P. Dhakal, D. L. Duong, Jubok Lee, Honggi Nam, Minsu Kim, Min Kan, Y. Hee Leea, and Jeongyong Kim, Nanoscale **6**, 13028 (2014).
[51] The two-dimensional density of states for band $E_n(\mathbf{K})$ can be calculated as $\mathrm{DOS}(E) = \frac{1}{2\pi^2} \int_{l(E)} \frac{dl}{|\nabla_{\mathbf{K}} E_n(\mathbf{K})|}$, where $l(E)$ is contour of constant energy $E_n(\mathbf{K}) = E$.
[52] S. L. Li, H. Miyazaki, H. Song, H. Kuramochi, S. Nakaharai, and K. Tsukagoshi, ACS Nano **6**, 7381 (2012).
[53] C. C. Shen, Y. T. Hsu, L. J. Li, and H. L. Liu, Appl. Phys. Express **6**, 125801 (2013).
[54] B. Mukherjee, F. Tseng, D. Gunlycke, K. K. Amara, G. Eda, and E. Simsek, Opt. Mater. Express **5**, 447 (2015).
[55] R. R. Gerhardts and V. Gudmundsson, Solid State Commun. **67**, 845 (1988).
[56] A. Manolescu and R. R. Gerhardts, Phys. Rev. B **56**, 9707 (1997).